Near-Field Signal Processing: Unleashing the Power of Proximity

Ahmet M. Elbir[1], *Senior Member, IEEE,* Özlem Tuğfe Demir[2], *Member, IEEE,* Kumar Vijay Mishra[3], *Senior Member, IEEE,* Symeon Chatzinotas[1], *Fellow, IEEE* and Martin Haardt[4], *Fellow, IEEE*

[1]University of Luxembourg, Luxembourg

[2] TOBB University of Economics and Technology, Turkey

[3]United States DEVCOM Army Research Laboratory, Adelphi, USA

[4]Ilmenau University of Technology, Ilmenau, Germany

E-mail: ahmetmelbir@ieee.org, ozlemtugfedemir@etu.edu.tr, kvm@ieee.org, symeon.chatzinotas@uni.lu, martin.haardt@tu-ilmenau.de

Abstract

After nearly a century of specialized applications in optics, remote sensing, and acoustics, the near-field (NF) electromagnetic propagation zone is experiencing a resurgence in research interest. This renewed attention is fueled by the emergence of promising applications in various fields such as wireless communications, holography, medical imaging, and quantum-inspired systems. Signal processing within NF sensing and wireless communications environments entails addressing issues related to extended scatterers, range-dependent beampatterns, spherical wavefronts, mutual coupling effects, and the presence of both reactive and radiative fields. Recent investigations have focused on these aspects in the context of extremely large arrays and wide bandwidths, giving rise to novel challenges in channel estimation, beamforming, beam training, sensing, and localization. While NF optics has a longstanding history, advancements in NF phase retrieval techniques and their applications have lately garnered significant research attention. Similarly, utilizing NF localization with acoustic arrays represents a contemporary extension of established principles in NF acoustic array signal processing. This article aims to provide an overview of state-of-the-art signal processing techniques within the NF domain, offering a comprehensive perspective on recent advances in diverse applications.

I. Introduction

Electromagnetic (EM) fields generated by an antenna create distinct spatial regions, each with unique characteristics [1]. Closest to the antenna surface is the near-field (NF) region, which is divided into reactive and radiative sub-regions, as illustrated in Fig. 1. The reactive NF, immediately adjacent to the antenna, is dominated by fields that rapidly diminish with distance and become negligible beyond a boundary of approximately λ/π, where λ is the operating wavelength. Beyond this boundary lies the

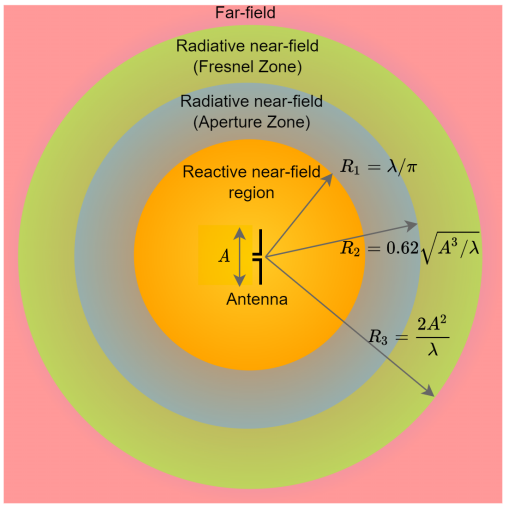

Fig. 1. EM field regions of an antenna of size A for the signal wavelength λ. The reactive NF is immediately adjacent to the antenna and becomes negligible at $R_1 = \lambda/\pi$. Beyond this boundary lies the radiative NF, itself split into two regions. The first part, known as the aperture zone, extends from R_1 to $R_2 = 0.62\sqrt{A^3/\lambda}$. The second part of the radiative NF is the Fresnel region, stretching from R_2 to $R_3 = 2A^2/\lambda$.

radiative NF, itself split into two regions. The first part, known as the aperture zone, extends from the reactive NF to approximately $0.62\sqrt{A^3/\lambda}$, where A is the antenna's maximum linear size. In this zone, the reactive fields are insignificant, the wavefront is quasi-planar, field strength remains nearly constant with distance, and the field amplitude distribution mirrors that of the antenna aperture. The second part of the radiative NF is the Fresnel region, stretching from $0.62\sqrt{A^3/\lambda}$ to $2A^2/\lambda$. In this region, the radiation pattern begins to form, but its shape depends on the distance from the antenna. This is due to changing phase relationships and varying field amplitude ratios between different antenna elements as distance increases.

As the observation point moves away from the antenna, the field amplitude initially oscillates before steadily decaying. At infinite distance, this attenuation becomes inversely proportional to the distance. Additionally, as distance increases, the phase and amplitude relationships between the fields from individual antenna elements gradually stabilize, and the angular distribution of the field becomes independent of distance. The outer boundary of the Fresnel zone, typically at $2A^2/\lambda$, marks the start of the far-field (FF) region, where the field distribution depends solely on the observation angle, and the field strength diminishes proportionally with distance. In this region, the EM wave's phase front is spherical, though it appears planar within small angles. The internal parameters of the antenna relate to both reactive and radiative fields, while external parameters are concerned solely with the radiated EM waves.

For much of its history, signal processing focused on FF applications, particularly in telecommunications, radar, and broadcasting, where the signals of interest were typically assumed to propagate over long distances with relatively simple wavefront characteristics. However, the unique NF properties were known for quite some time. Heinrich Hertz was among the first to observe that the field of a radiating dipole decays inversely with the third power of range at very close distances, rather than the inverse linear dependence observed in the FF. As a result, the field close to the dipole is significantly stronger than what one might expect from a simple extrapolation of the FF value. In 1909, Arnold Sommerfeld calculated the impact of NF perturbations on the radiation characteristics of a dipole antenna situated near the ground.

NF optics began to take shape in the late 1920s, driven by the need to surpass the diffraction limit in microscopy, enabling the visualization of structures at a nanometer scale [2]. This early work laid the groundwork for modern techniques such as NF scanning optical microscopy (NSOM) [3], with more recent applications in Raman spectroscopic imaging [4] and computational imaging [5]. In the field of acoustics, the 1980s marked the beginning of a focused effort on NF applications, where sound waves interact with objects in close proximity, leading to advances in technologies like NF acoustic holography [6], direction finding [7], underwater 3-D localization [8], NF sonar [9], beamforming [10, 11], and sensor array optimization [12]. In ultrasound imaging, beamforming is usually performed via using wideband signals in NF [13, 14].

In radar remote sensing, NF imaging has a rich research heritage dating back to the 1990s, particularly in applications like ground-penetrating radar, through-the-wall imaging, and synthetic aperture interferometry [15]. Recent NF radar signal processing applications focus on direction-of-arrival (DoA) estimation [16], localization [17], and correlated/coherent source localization [18, 19]. One of the major issues has been to derive the performance bounds, e.g., Cramér-Rao bounds (CRB) for parameter estimation in NF scenarios [20, 21]. The consideration of a NF signal model makes the parameter estimation more challenging especially when the received signal includes both NF and FF signals [22, 23]. In order to estimate the DoA and the range information of the NF sources, a well-known technique is to employ a multiple signal classification (MUSIC) algorithm over both direction and range dimensions [24]. As MUSIC is a subspace-based approach, it fails when the signals are coherent, i.e., fully correlated. In such cases, maximum-likelihood (ML) [18] or compressed sensing (CS) [19] approaches can be employed. Relying on the high order statistics (HOS) of the array data, fourth order cumulants are also used [25, 26].

More recently, the evolution of array signal processing in wireless communications is moving towards the use of small, densely packed sensors to create extremely large aperture arrays (ELAA), which

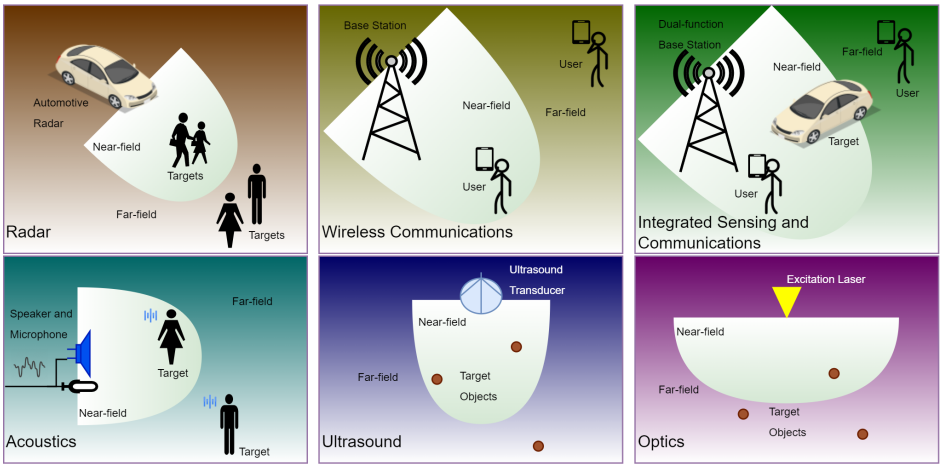

Fig. 2. Applications of NF signal processing on radar, communications, acoustics, ultrasound and optics.

significantly enhance angular resolution and beamforming gain [27, 28]. Particularly, with the advent of sixth-generation (6G) networks, there is a notable adoption of ELAAs or surfaces, coupled with the exploitation of higher frequency bands like terahertz (THz) frequencies, shifting the EM diffraction field from the FF region to the NF. The extended array aperture and shorter wavelengths in the NF region, where the receiver is closer to the transmitter than the Fraunhofer distance [29], result in non-planar signal wavefronts. With larger array apertures and frequencies, the NF range can extend tens to hundreds of meters, crucial for communication system design [30–32]. For instance, an antenna array of 1-m aperture operating at 30 GHz yields a NF region of up to 200 meters, which is critical for system design in communication environments [32]. In this context, spherical wavefront considerations become paramount in beamforming design, enabling signal focusing at specific 3-D locations rather than traditional FF beamsteering towards specific angles. The ELAA system facilitates not only directional signal reception but also transmitter localization, distinguishing it from conventional FF designs. However, exploiting the NF region presents both opportunities and challenges in communication [31] and sensing [21] applications. Beamforming in NF leverages depth information to enhance spatial multiplexing, catering to users at varying distances within the same direction. Additionally, high-resolution sensing and localization are imperative in the NF, necessitating innovative communication strategies. Furthermore, in large arrays operating at high bandwidths, the frequency-dependent array response poses challenges to conventional beamforming, necessitating adaptive strategies for optimized beamforming gains [33].

Communications channel estimation in NF involves the reconstruction of the channel via estimating the complex channel gain as well as the direction and the range information of the dominant signal

paths. In contrast to the radar scenario, the received signal includes several non-line-of-sight (NLoS) reflections, which may be in the NF of the receiver [34, 35]. This poses challenges to model the received signal for communications, wherein the aim is to improve the communication rate, rather than estimating the location of the user. In beamforming, the aim is to optimize the beamformer weights to maximize the communication rate. By taking into account the spherical-wave model of the received path signals, various techniques have been adopted for beamforming, e.g., CS [36] and orthogonal matching pursuit (OMP) [37, 38]. Combined with radar, integrated sensing and communications (ISAC) is a new paradigm to effectively use the system resources on a common platform for simultaneously performing radar sensing of targets or users as well as communication with the users [39, 40]. In this respect, recent research also includes NF signal processing techniques to provide both sensing and communication functionalities, such as beamforming [36] as well as user/target localization [39].

The intent of this article is to encapsulate the *recent* advancements in NF signal processing techniques. Notably, there is a distinct absence of surveys encapsulating signal processing strategies for the NF and acquainting with the nuances and challenges of this burgeoning field. Lately, literature on NF signal processing involves short/extensive surveys [30–32] mainly on wireless communications while there is a substantial gap for an overview of NF signal processing techniques in radar, acoustics, ultrasound, and optics (Fig. 2). This article aims to present a synopsis of the state-of-the-art signal processing techniques in the NF with a focus on array processing and its contemporary applications.

II. NF Signal Model

Consider a uniform linear array (ULA) with N antenna elements and inter-element spacing d that receives signals emitted from K sources. We define $s_k(t) \in \mathbb{C}$ as the emitted signal from the k-th source with the direction of θ_k at time t. Then, the observation model at the n-th antenna element is given by

$$y_n(t) = \sum_{k=1}^{K} s_k(t) e^{-\mathrm{j}2\pi f_c \tau_{n,k}} + e_n(t), \tag{1}$$

where f_c is the carrier frequency and $e_n(t) \in \mathbb{C}$ denotes the additive white Gaussian noise, and normlized time delay $\tau_{n,k}$ is associated with the the k-th source signal propagation time among the antennas as

$$\tau_{n,k} = \frac{r_k}{f_c \lambda} \left(\sqrt{1 + \frac{n^2 d^2}{r_k^2} - \frac{2nd \sin\theta_k}{r_k}} - 1 \right), \tag{2}$$

where λ is the signal wavelength and r_k denotes the range of the k-th source. Depending on propagation distance, the source location may be regarded in the reactive, radiative or FF of the array:

- The reactive NF starts from the array to $0.62\sqrt{D^3/\lambda}$, where D denotes the array aperture, and it is defined as $D = (N-1)d$ for a ULA [41].

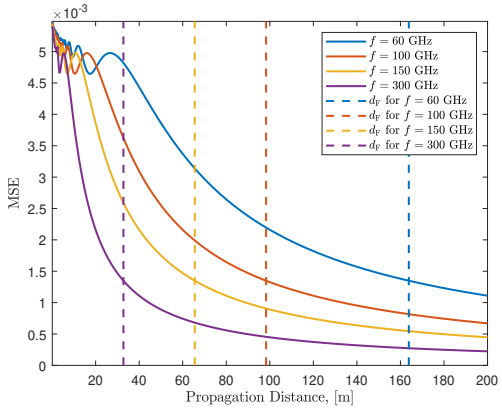

Fig. 3. MSE for the difference of NF and FF signal model for a ULA of $N = 256$ elements on various frequencies.

- The radiative NF (i.e., Fresnel region) extends from the reactive NF to FF, i.e., $0.62\sqrt{D^3/\lambda} < r < \frac{2D^2}{\lambda}$ [30]. It is in this region that the time delay $\tau_{n,k}$ can be approximated by using a Taylor series expansion as

$$\tau_{n,k} = -\frac{1}{2\pi f_c}\left(\omega_k n + \kappa_k n^2 + O\left(\frac{d^2}{r_k^2}\right)\right), \tag{3}$$

where $\omega_k = \frac{2\pi d \sin\theta_k}{\lambda}$ and $\kappa_k = -\frac{\pi d^2 \cos^2\theta_k}{\lambda r_k}$. Then, by neglecting $O\left(\frac{d^2}{r_k^2}\right)$ in the time delay expression, the observation model in (1) becomes

$$y_n(t) = \sum_{k=1}^{K} s_k(t) e^{\mathrm{j}(\omega_k n + \kappa_k n^2)} + e_n(t). \tag{4}$$

- The FF region starts after $d_{\mathrm{F}} = \frac{2D^2}{\lambda}$, which is called the Fraunhofer distance, and it covers $r > \frac{2D^2}{\lambda}$, wherein the plane wavefront can be approximated as planar with a maximum spherical-induced phase-shift of $\pi/8$ across the antennas [29]. Fig. 3 shows the mean-squared error (MSE) for the difference of NF and FF signal models for various frequencies and d_{F}. We can see that this MSE decreases as the propagation distance d increases and becomes negligible after $d > d_{\mathrm{F}}$.

In a compact form, the $N \times 1$ observation vector $\mathbf{y}(t) \in \mathbb{C}^N$ can be expressed as

$$\mathbf{y}(t) = \mathbf{A}\mathbf{s}(t) + \mathbf{e}(t), \tag{5}$$

where $\mathbf{y}(t) = [y_1(t), \cdots, y_N(t)]^{\mathsf{T}}$, $\mathbf{e}(t) = [e_1(t), \cdots, e_N(t)]^{\mathsf{T}}$ and $\mathbf{s}(t) = [s_1(t), \cdots, s_K(t)]^{\mathsf{T}}$. Here, $\mathbf{A} = [\mathbf{a}(r_1, \theta_1), \cdots, \mathbf{a}(r_K, \theta_K)] \in \mathbb{C}^{N \times K}$ denotes the array response, and $\mathbf{a}(r_k, \theta_k) \in \mathbb{C}^N$ represents the steering vector corresponding to the k-th source as

$$\mathbf{a}(r_k, \theta_k) = \left[1, e^{\mathrm{j}(\omega_k + \kappa_k)}, \cdots, e^{\mathrm{j}(\omega_k (N-1) + \kappa_k (N-1)^2)}\right]^{\mathsf{T}}. \tag{6}$$

III. NF RADAR

The localization of the radar signals in the proximity of antenna array has been extensively studied. This includes the estimation of the DoA angles as well as the range of the emitting source direction. Practical radar applications involve several challenging scenarios, which requires advanced signal processing techniques for accurate parameters estimation. Unlike FF scenario, the array response is range-dependent, which should be taken into account for source parameter estimation. Range-dependent beampattern is also observed in some far-field applications such as frequency diverse array (FDA) radars [42] and quantum Rydberg arrays [43]. However, the wavefront is not spherical in these applications.

A. DoA Estimation and Localization

Subspace-based techniques, e.g., the MUSIC algorithm [24], have been widely used for NF DoA estimation and localization. Define $\mathbf{R} \in \mathbb{C}^{N\times N}$ as the sample covariance matrix of the array output $\mathbf{y}(t)$ as

$$\mathbf{R} = \frac{1}{T}\sum_{t=1}^{T} \mathbf{y}(t)\mathbf{y}^{\mathsf{H}}(t), \tag{7}$$

where T is the number of data snapshots collected from the array. Then, the MUSIC algorithm for NF DoA and range estimation is performed by finding the peak values of the following MUSIC spectra [17], i.e.,

$$P(\theta, r) = \frac{1}{\mathbf{a}^{\mathsf{H}}(\theta, r)\mathbf{U}_{\mathrm{N}}\mathbf{U}_{\mathrm{N}}^{\mathsf{H}}\mathbf{a}(\theta, r)}, \tag{8}$$

where $\mathbf{U}_{\mathrm{N}} \in \mathbb{C}^{N\times(N-K)}$ denotes the noise subspace eigenvectors, which can be obtained from the eigenvalue decomposition of $\mathbf{R}$ as $\mathbf{R} = \mathbf{U}\mathbf{\Lambda}\mathbf{U}^{\mathsf{H}}$, where $\mathbf{\Lambda} \in \mathbb{C}^{K\times K}$ includes the eigenvalues of $\mathbf{R}$ in descending order and $\mathbf{U} = [\mathbf{U}_{\mathrm{S}},\ \mathbf{U}_{\mathrm{N}}] \in \mathbb{C}^{N\times N}$ is composed of the eigenvectors corresponding to the signal and noise subspaces, respectively.

B. Mixed NF and FF Source Localization

In some practical applications, the signal received by the array is a mixture of FF and NF sources [23]. Fig. 4(a) shows the array beampattern for mixture of FF and NF targets. For example, in high frequency (HF) radar, the NF multipaths have strong effects compared to very/ultra high frequency (V/U-HF) bands such that the received signal is composed of a FF source signal as well as its NF reflections [19]. Assume that there exist K_{F} FF and K_{N} NF emitting sources, for which the array output is given by

$$\mathbf{y}(t) = \sum_{k=1}^{K_{\mathrm{F}}} \mathbf{a}(\theta_k)s_k(t) + \sum_{k=K_{\mathrm{F}}+1}^{K} \mathbf{a}(\theta_k, r_k)s_k(t) + \mathbf{e}(t), \tag{9}$$

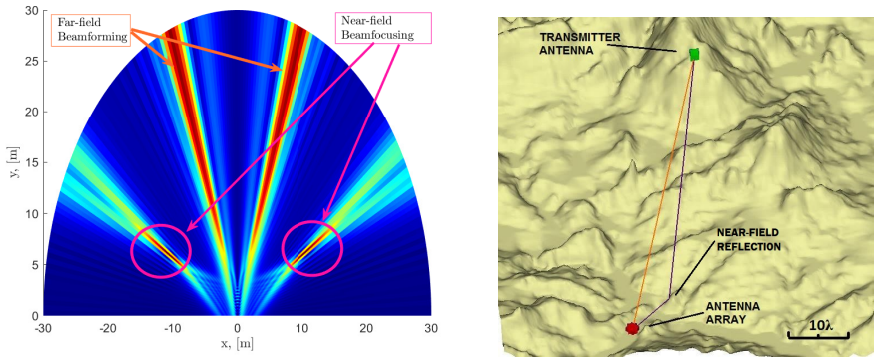

(a) (b)

Fig. 4. Mixed FF and NF scenario. (a) Array beampattern for the mixture of FF beamforming and NF beamfocusing. (b) Coherent mixture FF and NF signals.

where $K = K_{\mathrm{F}} + K_{\mathrm{N}}$ and $\mathbf{a}(\theta_k) \in \mathbb{C}^N$ denotes the FF steering vectors for $k \in \{1, \cdots, K_{\mathrm{F}}\}$. In this scenario, the MUSIC algorithm can be employed in a two-stage scheme to sequentially estimate FF and NF parameters. In [22], two different special cumulant matrices are designed for this purpose. Consider a ULA with $N = 2\bar{N} + 1$ elements and let 0-th antenna be phase reference of the array. Then, the fourth-order cumulant of the array outputs can be expressed as

$$\mathrm{cum}\{y_p(t), y_{-p}^*(t), y_q(t), y_{-q}(t)\} = \sum_{k=1}^{K} c_{s_k} e^{\mathrm{j}(2p\omega_k - 2q\omega_k)}, \tag{10}$$

where $p, q \in [-\bar{N}, \bar{N}]$, and $c_{s_k} = \mathrm{cum}\{s_k(t), s_k^*(t), s_k^*(t), s_k(t)\}$ is the kurtosis of the k-the signal [17]. Define $\bar{p} = p + \bar{N} + 1$ and $\bar{q} = q + \bar{N} + 1$. The $(\bar{p}, \bar{q})$-th element of the cumulant matrix $\mathbf{C}_1 \in \mathbb{C}^{N \times N}$ is

$$\begin{aligned}[\mathbf{C}_1]_{\bar{p},\bar{q}} =& \mathrm{cum}\{y_{\bar{p}-\bar{N}-1}(t), y_{-\bar{p}+\bar{N}+1}^*(t), y_{\bar{q}-\bar{N}-1}^*(t), y_{-\bar{q}+\bar{N}+1}(t)\} \\ =& \sum_{k=1}^{K} c_{s_k} e^{\mathrm{j}(2(\bar{p}-\bar{N}-1)\omega_k - 2(\bar{q}-\bar{N}-1)\omega_k)}.\end{aligned} \tag{11}$$

We can write $\mathbf{C}_1$ in a compact form as $\mathbf{C}_1 = \mathbf{B}_1 \mathbf{C}_s \mathbf{B}_1^{\mathsf{H}}$, where the virtual steering matrix and vectors are defined as $\mathbf{C}_s = \mathrm{diag}\{c_{s_1}, \cdots, c_{s_K}\} \in \mathbb{C}^{K \times K}$, and $\mathbf{B}_1 = [\mathbf{b}_1(\omega_1), \cdots \mathbf{b}_1(\omega_K)]$, where $\mathbf{b}_1(\omega_k) = \left[e^{-\mathrm{j}2\bar{N}\omega_k}, \cdots, e^{\mathrm{j}2\bar{N}\omega_k}\right]^{\mathsf{T}} \in \mathbb{C}^N$ for $k = 1, \cdots, K$. By computing the MUSIC spectra based on the noise subspace eigenvectors of $\mathbf{C}_1$, the DoA information ω_k for $k \in \{1, \cdots, K_{\mathrm{F}}\}$ can be obtained via

$$P(\omega) = \frac{1}{\mathbf{b}_1^{\mathsf{H}}(\omega) \mathbf{U}_{\mathrm{N}_1} \mathbf{U}_{\mathrm{N}_1}^{\mathsf{H}} \mathbf{b}_1(\omega)}, \tag{12}$$

where $\mathbf{U}_{\mathrm{N}_1} \in \mathbb{C}^{N \times (N-K)}$ denotes the noise subspace eigenvector matrix of $\mathbf{C}_1$. In order to estimate κ_k, another cumulant matrix $\mathbf{C}_2 \in \mathbb{C}^{(4\bar{N}+1) \times (4\bar{N}+1)}$ is constructed as $\mathbf{C}_2 = \begin{bmatrix} \mathbf{C}_{2,1} & \mathbf{C}_{2,2} \\ \mathbf{C}_{2,3} & \mathbf{C}_{2,4} \end{bmatrix}$, which

can be written as $\mathbf{C}_2 = \mathbf{B}_2\mathbf{C}_s\mathbf{B}_2^{\mathsf{H}}$, where $\mathbf{B}_2 = [\mathbf{b}_2(\omega_1,\kappa_1),\cdots,\mathbf{b}_2(\omega_K,\kappa_K)] \in \mathbb{C}^{(4\bar{N}+1)\times K}$, and $\mathbf{b}_2(\omega_k,\kappa_k) = \mathbf{b}_2(\omega_k)\mathbf{b}_2(\kappa_k) \in \mathbb{C}^{4\bar{N}+1}$ (See [22] for the computation of $\mathbf{b}_2(\omega_k)$, $\mathbf{b}_2(\kappa_k)$ and $\mathbf{C}_{2,i}$, $i = 1,\cdots,4$). Then, by substituting the estimated ω_k into $\mathbf{b}_2(\omega_k,\kappa_k)$, the following MUSIC spectra reveals the range-dependent source parameters κ_k for $k \in \{K_{\mathrm{F}}+1,\cdots,K_{\mathrm{F}}+K_{\mathrm{N}}\}$, i.e.,

$$P(\kappa) = \frac{1}{\mathbf{b}_2^{\mathsf{H}}(\omega,\kappa)\mathbf{U}_{\mathrm{N}_2}\mathbf{U}_{\mathrm{N}_2}^{\mathsf{H}}\mathbf{b}_2(\omega,\kappa)}, \tag{13}$$

where $\mathbf{U}_{\mathrm{N}_2} \in \mathbb{C}^{(4\bar{N}+1)\times(4\bar{N}+1-K)}$ denotes the noise subspace eigenvector matrix of $\mathbf{C}_2$.

The aforementioned technique require multiple steps to sequentially estimate the DoA and range parameters of the mixture signals. Instead, more efficient techniques have been introduced in the literature by exploiting the special geometry/structure of the antenna arrays, e.g., subarrayed ULA [44] and nested array [23]. Apart from these model-based approaches, data-driven techniques have also been devised [45].

C. Correlated/Coherent Signal Estimation

In practice, the source signals are not always uncorrelated because of the received reflections from the objects which can be located in the FF or NF of the antenna array. In the most extreme scenario, the signal are coherent, i.e., fully correlated, such that the covariance matrix of the received signal turns out to be rank-deficient [18]. For example, in multipath scenario, the emitted signals from FF or NF sources are scattered from the objects in the vicinity of the antenna array as shown in Fig. 4(b). Consider a single FF source signal $s_1(t)$ (i.e., $K_{\mathrm{F}} = 1$), which is then reflected from $K_{\mathrm{N}} = K-1$ reflection points in the NF of the array. Thus, the reflected signals are coherent with $s_1(t)$, i.e, $s_k(t) = \zeta_k s_1(t)$ for $k \in \{2,\cdots,K\}$ and $\zeta_k \in \mathbb{C}$. Then, the mixture model in (9) is written for coherent signals as

$$\mathbf{y}_c(t) = \mathbf{a}(\theta_1)s_1(t) + \sum_{k=2}^{K}\mathbf{a}(\theta_k,r_k)s_1(t) + \mathbf{e}(t). \tag{14}$$

Since the covariance matrix of $\mathbf{y}_c(t)$ is rank-1, the subspace-based methods fail to resolve source angle and ranges. In [19], a calibration-based approach is presented to estimate the angle and range parameters of mixture signals. Specifically, the NF signal components are first treated as disturbance signals to be calibrated, and the FF DoA angle is estimated. Then, the NF parameters are found. By exploiting the coherent signal model, the observation in (14) can be written as

$$\mathbf{y}(t) = \mathbf{a}(\theta_1)s_1(t)(1+\beta_2+\beta_3+\cdots+\beta_K) + \mathbf{e}(t), \tag{15}$$

where $\beta_k = \frac{s_k(t)}{s_1(t)}$ ($k \in \{2,\ldots,K\}$) is a direction-dependent coefficient. Then, the array model for FF is

$$\mathbf{y}(t) = \mathbf{\Gamma}\mathbf{a}(\theta_k)s_1(t) + \mathbf{e}(t), \tag{16}$$

where $\mathbf{\Gamma} = \text{diag}\{\gamma_1, \cdots, \gamma_N\} \in \mathbb{C}^{N\times N}$ is a direction-dependent matrix representing the impact of NF signals as disturbances. As a result, the FF DoA angles can estimated with the knowledge of $\mathbf{\Gamma}$, which can be designed via a calibration technique. Define $\tilde{\mathbf{A}} = \left[\tilde{\mathbf{a}}(\tilde{\theta}_1), \cdots, \tilde{\mathbf{a}}(\tilde{\theta}_C)\right] \in \mathbb{C}^{N\times C}$ as the set of measurements collected during calibration process for C different DoA angles. Assume that the calibration data is collected at the DoA angles $\tilde{\Theta} = \{\tilde{\theta}_1, \cdots, \tilde{\theta}_C\}$ uniformly in $[-\pi/2, \pi/2]$. Then, the elements of the calibration matrix $\mathbf{\Gamma}_c$ at the c-th calibration angle $\tilde{\theta}_c$ can be found as $\gamma_{n,c} = \frac{[\tilde{\mathbf{a}}(\tilde{\theta}_c)]_n}{[\mathbf{a}(\theta_c)]_n}$ for $c = 1, \cdots, C$ and $n = 1, \cdots, N$. Then, the FF DoA angle θ_1 can be estimated from the following MUSIC spectra evaluated at $\tilde{\Theta}$ i.e.,

$$P(\theta_c) = \frac{1}{\mathbf{a}^{\mathsf{H}}(\theta_c)\tilde{\mathbf{U}}_{\mathrm{N}}\tilde{\mathbf{U}}_{\mathrm{N}}^{\mathsf{H}}\mathbf{a}(\theta_c)}, \tag{17}$$

where $\tilde{\mathbf{U}}_{\mathrm{N}} \in \mathbb{C}^{N\times(N-1)}$ is the noise subspace eigenvector matrix for the covariance of $\mathbf{y}(t)$ in (14). Once the FF signal are obtained, the array output in (14) is transformed to the FF domain to perform angle estimation of the NF signals by employing a near-to-far transformation (NFT) matrix $\mathbf{T} \in \mathbb{C}^{N\times N}$, i.e., $\mathbf{A}_{\mathrm{FF}} = \mathbf{T}\mathbf{A}_{\mathrm{NF}}$, where $\mathbf{A}_{\mathrm{FF}} \in \mathbb{C}^{N\times C}$ and $\mathbf{A}_{\mathrm{NF}} \in \mathbb{C}^{N\times C}$ denote the collected FF and NF calibration measurements. Then, the transformed array output is given by

$$\mathbf{y}_{\mathrm{nf}}(t) = \mathbf{T}\mathbf{y}(t) = \underbrace{\mathbf{T}\mathbf{a}(\theta_1)s(t) + \mathbf{T}\mathbf{e}(t)}_{\text{distortions}} + \underbrace{\sum_{k=2}^{K} \mathbf{T}\mathbf{a}(\theta_k, r_k)s_1(t)}_{\text{desired NF signal}}, \tag{18}$$

where the FF signal behave like distortion. The transformed signal in (18) is still rank-deficient. To alleviate this, forward-backward spatial smoothing (FBSS) technique [46] to construct a full-rank covariance matrix. Then, the DoA angles of the desired signals can be obtained via FF MUSIC algorithm based on the covariance of $\mathbf{y}_{\mathrm{nf}}(t)$. Finally, the estimation of the ranges of the NF signals can be performed via sparsity-based techniques by substituting the estimated FF and NF DoA angles [19].

IV. NF Wireless Communications

NF signal processing is an emerging area of research in wireless communications, driven by advancements in mmWave [47, 48] and THz [34, 49] technologies. For instance, mmWave massive MIMO systems, which involve a very large number of antennas (e.g., > 128) and operate at high frequencies (e.g., > 30 GHz), can have a Fraunhofer distance extending up to hundreds of meters. In such cases, NF signal processing becomes crucial for performing key communication tasks such as channel estimation, beamforming, and resource allocation.

A. Channel Estimation

Consider K single-antenna users and L effective scatterers between each user and the BS. When all the effective scatterers between the BS and a particular user are located within the radiative NF of the BS, the channel between the BS and user k can be expressed as

$$\mathbf{h}_k = \sum_{l=1}^{L} \alpha_{k,l} \mathbf{a}(\theta_{k,l}, r_{k,l}), \tag{19}$$

where $\alpha_{k,l}$ is the complex gain of the l-th path. The $\theta_{k,l}$ and $r_{k,l}$ are the corresponding angle and distance. To estimate the users' channels, the BS receives pilot sequences sent by the users during the training interval. To facilitate channel estimation and avoid interference, we assume that users are assigned orthogonal pilot sequences. This allows us to focus on a single user's received pilot signal (omitting the user index k), which is given by

$$\mathbf{y} = \sqrt{\rho}\mathbf{A}\mathbf{h} + \mathbf{n}, \tag{20}$$

where $\mathbf{y}$ is obtained after correlating the received signals with the pilot sequence of the user of interest, and ρ is the pilot signal-to-noise ratio (SNR). The matrix $\mathbf{A} \in \mathbb{C}^{N_{\mathrm{RF}} \times N}$ represents the analog combining matrix, where the BS employs a hybrid beamforming architecture with N_{RF} RF chains. Each entry of $\mathbf{A}$ has a modulus of $1/\sqrt{N}$ [50]. The independent additive noise is denoted by $\mathbf{n} \sim \mathcal{N}_{\mathbb{C}}(\mathbf{0}, \mathbf{I}_N)$.

To leverage the sparse characteristics of high-frequency channels when L is relatively small, we can utilize OMP-type algorithms with codebooks specifically designed to account for the NF spherical wavefront [34, 49]. For a good performance in the OMP algorithm, the dictionary matrix should exhibit low column coherence, meaning the magnitude of the maximum pairwise inner product between different columns is minimized. In FF scenarios, the dictionary matrix can be constructed using the columns of a discrete Fourier transform (DFT) matrix that correspond to FF array steering vectors. Conversely, for the NF case, a common approach to dictionary construction is the polar-domain design [50], which aims to achieve low column coherence, which is given as

$$\mu = \max_{p \neq q} \left| \mathbf{a}^{\mathsf{H}}(\theta_p, r_p)\, \mathbf{a}(\theta_q, r_q) \right|, \tag{21}$$

where p and q are the column indices of the dictionary. The absolute value of the inner product is

$$\left| \mathbf{a}^{\mathsf{H}}(\theta_p, r_p)\, \mathbf{a}(\theta_q, r_q) \right| = \left| \sum_{n=-\bar{N}}^{\bar{N}} e^{-\mathrm{j}\frac{2\pi}{\lambda}\left(dn(\sin\theta_q - \sin\theta_p) + d^2 n^2 \left(\frac{\cos^2\theta_p}{2r_p} - \frac{\cos^2\theta_q}{2r_q} \right) \right)} \right|, \tag{22}$$

where we have considered an ULA with $N = 2\bar{N} + 1$ elements and 0-th antenna being phase reference of the array. In polar-domain dictionary design, both angular and distance sampling are performed. For

angular sampling, we consider two arbitrary locations where $\frac{\cos^2\theta}{r} = \frac{1}{\phi}$, with ϕ representing a constant corresponding to the distance ring ϕ. On this distance ring, the nulls are obtained by sampling the angles

$$\theta = \arcsin\left(\frac{n\lambda}{Nd}\right), \quad n = 0, \pm 1, \pm 2, \ldots, \pm\left\lfloor \frac{Nd}{\lambda} \right\rfloor. \tag{23}$$

For distance sampling, we focus on two arbitrary locations with the same angle. Using the Fresnel integral approximation of the summation in (22), one can derive that [50, Lemma 1], the distances should be sampled according to

$$r = \frac{1}{s}\frac{N^2 d^2 \cos^2\theta}{2\lambda\varepsilon^2}, \quad s = 0, 1, 2, \ldots, \tag{24}$$

where $\varepsilon > 0$ is a parameter that can be adjusted to guarantee a certain column coherence. For instance, to guarantee at most 0.5 of the maximum inner product (i.e., N), ε should be selected larger than 1.6.

The dictionary matrix $\mathbf{W}$ is constructed using the array steering vectors $\mathbf{a}(\theta, r)$, with angles and distances selected according to the previously described angular and distance sampling methods to achieve the desired column coherence. In Fig. 5(a), we compare the least squares (LS) channel estimator with the OMP algorithm using dictionaries designed with $\varepsilon = 1$ and $\varepsilon = 2$. The simulation parameters are as follows: $N = 256$, $N_{\mathrm{RF}} = 8$, and $\mathrm{SNR} = 10$ dB. As shown in the figure, as the pilot length increases, the normalized mean-squared error (NMSE) of all estimators decreases, with the OMP algorithm demonstrating superior performance when the pilot length is sufficiently large. This is because the OMP algorithm, combined with the polar-domain dictionary, effectively exploits both sparsity and the NF array steering vector structure, unlike the non-parametric LS estimator.

NF effects can also be observed in midband frequencies for extremely large-scale arrays [29]. At these frequencies, the sparsity may no longer exist. In such cases, the spatial correlation matrix can be utilized. When the full knowledge of the spatial correlation matrix is available, the optimal approach is to use the minimum mean-squared error (MMSE) estimator. However, acquiring the spatial correlation matrix becomes increasingly challenging, particularly as the array size grows. To improve upon the simplest LS alternative, one option for two-dimensional arrays is to leverage the low-rank characteristics of any plausible spatial correlation matrix, which is independent of specific user locations and only dependent on array geometry. The corresponding reduced-dimension LS (RS-LS) estimator can provide significantly better estimates than LS without requiring specific correlation matrix knowledge [51].

B. Beamforming vs. Beam-Focusing

Suppose a user has a line-of-sight (LoS) channel to the BS. If the user is situated in the FF of the BS and the BS employs maximum ratio transmission (MRT) precoding by adjusting the precoding vector

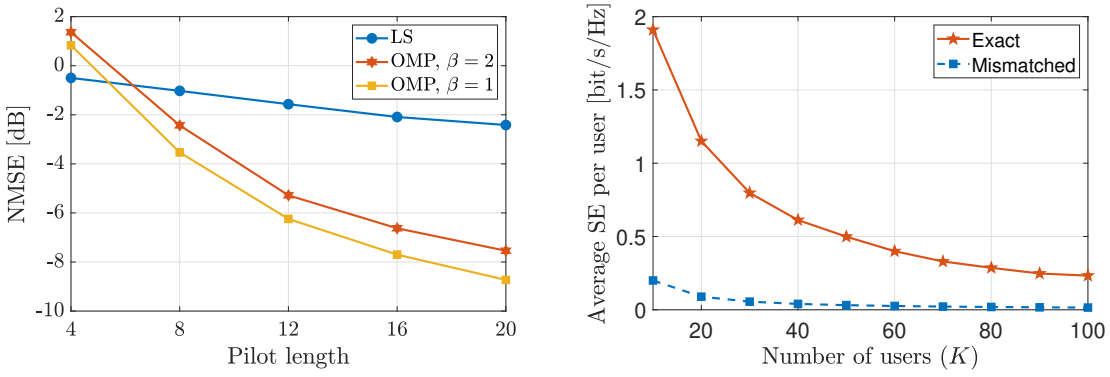

(a) (b)

Fig. 5. Channel estimation and SE performance. (a) NMSE versus pilot length for the LS and OMP-based channel estimators. (b) Average SE per user with exact NF channels and mismatched FF channels.

according to the user's FF array steering vector, the resulting beampattern exhibits a finite beamwidth across the angular domain. However, along the distance at the user's angle, the beampattern remains strong. On the other hand, if the user is located in the NF of the BS, there is both a finite beam width across the angular domain and a finite beam depth along the distance domain. This can be understood by analyzing the NF beampattern at a specific angle θ by computing the normalized array gain:

$$G(\theta, r) = \frac{1}{N} \left| \mathbf{a}^{\mathsf{H}}(\theta, r_0)\, \mathbf{a}(\theta, r) \right|, \tag{25}$$

where r_0 is the range of the user [31]. It can be shown that $G(\theta, r)$ can be approximated using Fresnel integrals $C(z) = \int_0^z \cos\left(\frac{\pi}{2}x^2\right) dx$ and $S(z) = \int_0^z \sin\left(\frac{\pi}{2}x^2\right) dx$ by

$$G(\theta, r) \approx \left| \frac{C(z) + \mathrm{j}S(z)}{z} \right|, \tag{26}$$

where $z = \sqrt{\frac{N^2 d^2 \sin^2\theta}{2\lambda} \left| \frac{1}{r_0} - \frac{1}{r} \right|}$. Since $\left| \frac{C(z)+\mathrm{j}S(z)}{z} \right|$ is a decreasing function for $z \in [0, 1.8]$ and it reduces to 0.5 when $z \approx 1.6$, there is a finite beam depth along the r axis, which defines the 3 dB beam depth. After some mathematical manipulations, it can be shown that if $r < r_{\mathrm{BD}}$ where $r_{\mathrm{BD}} = \frac{N^2 d^2 \sin^2\theta}{2\lambda z_{3\mathrm{dB}}^2}$, where $z_{3\mathrm{dB}} = 1.6$, the 3 dB beam depth (BD) is given as

$$\mathrm{BD}_{3\mathrm{dB}} = \frac{2 r_0^2 r_{\mathrm{BD}}}{r_{\mathrm{BD}}^2 - r_0^2}. \tag{27}$$

On the other hand, if $r_0 \geq r_{\mathrm{BD}}$, then the beam depth becomes infinity as in the FF case.

One of the significant implications of NF beam focusing is that multiple users can be simultaneously served by the BS, even if they are located along the same angle. This is not possible in the FF scenario, where nulling the interference between users is challenging. Due to the finite beam depth characteristics

of beam-focusing, it is feasible to spatially multiplex many users, a concept known as *massive spatial multiplexing* [52].

To exemplify massive spatial multiplexing, we consider the uplink of a multi-user MIMO system with K single-antenna users. Following [52, Sec. II.B], if one uses MMSE combining scheme, the spectral efficiency of the k-th user is given as

$$\mathrm{SE}_k = \log_2 \left(1 + p_k \mathbf{h}_k^{\mathsf{H}} \left(\sum_{i=1, i\neq k}^{K} p_i \mathbf{h}_i \mathbf{h}_i^{\mathsf{H}} + \sigma^2 \mathbf{I}_N \right)^{-1} \mathbf{h}_k \right), \tag{28}$$

where, p_k denotes the transmit power of the k-th user, and σ^2 represents the noise variance. In Fig. 5(b), we present the average SE per user for $N = 512$, $f_c = 30$ GHz, $p_k = 0.2$ W, and $\sigma^2 = -87$ dBm, which corresponds to a 100 MHz bandwidth [53]. K users are positioned at an angle of $\theta = 0$, with distances uniformly distributed between 20 and 500 meters. In the figure, the "exact" curve illustrates the SE derived using the precise NF LoS channels, while the "mismatched" curve represents the case where LoS channels are approximated by FF array steering vectors. As shown, approximating user channels as FF significantly reduces SE. This demonstrates that, despite identical path losses in both cases, utilizing NF channels leads to a considerable improvement in SE.

C. Wideband Processing and Beam-Squint

In wideband hybrid beamforming, the generated beam direction changes across the subcarriers compared to the central subcarrier. When the bandwidth is relatively large, e.g., in mmWave or THz designs, the beam direction squints especially at the high-end and low-end subcarriers. This phenomenon is called beam-squint [54]. For instance, consider two users/targets located in the FF and NF at the broadside direction. In the FF, the angular deviation due to beam-squint is roughly 6° (0.4°) for 300 GHz with 30 GHz (60 GHz with 1 GHz) bandwidth, respectively. However, NF beam-squint has approximately $(6^\circ, 10\mathrm{m})$ angular and range deviation for a target/user located at 20 m distance for 300 GHz with 30 GHz bandwidth. Fig. 6(a) shows the array beampattern in the presence of NF beam-squint.

Consider the array steering vector in (6), which can be rewritten in terms of the distance between the k-th source and the n-th antenna, $r_k^{(n)}$, as

$$\mathbf{a}(\vartheta_k, r_k) = [e^{-\mathrm{j}2\pi \frac{d}{\lambda} r_k^{(1)}}, \cdots, e^{-\mathrm{j}2\pi \frac{d}{\lambda} r_k^{(N)}}]^{\mathsf{T}}, \tag{29}$$

where $\vartheta_k = \sin\theta_k$ and $r_k^{(n)} = \sqrt{r_k^2 + 2(n-1)^2 d^2 - 2r_k(n-1)d\vartheta_k}$, which can be approximated [29, 32] as $r_k^{(n)} \approx r_k - (n-1)d\vartheta_k + (n-1)^2 d^2 \Upsilon_k$, where $\Upsilon_k = \frac{1-\vartheta_k^2}{2r_k}$. Then, we can rewrite (29) as $\mathbf{a}(\vartheta_k, r_k) \approx e^{-\mathrm{j}2\pi \frac{f_c}{c_0} r_k} \tilde{\mathbf{a}}(\vartheta_k, r_k)$, where the n-th element of $\tilde{\mathbf{a}}(\vartheta_k, r_k) \in \mathbb{C}^N$ is

$$[\tilde{\mathbf{a}}(\vartheta_k, r_k)]_n = e^{\mathrm{j}2\pi \frac{f_c}{c_0}((n-1)d\vartheta_k - (n-1)^2 d^2 \Upsilon_k)}. \tag{30}$$

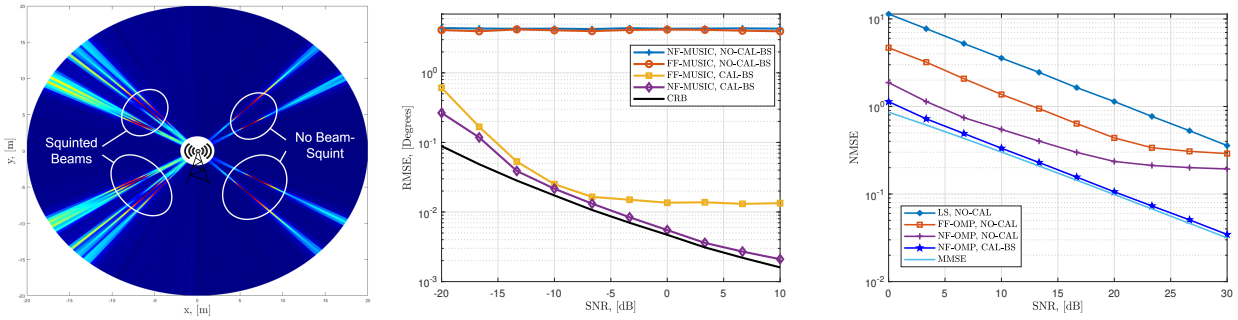

(a) (b) (c)

Fig. 6. Beam-squint calibration in NF: (a) Array beampattern in the presence of NF beam-squint. (b) DoA estimation RMSE in NF radar. (b) Channel estimation in NF communications.

Due to beam-squint, the generated beam toward (ϑ_k, r_k) deviates to the spatial location $(\bar{\vartheta}_{m,k}, \bar{r}_{m,k})$ at the m-th subcarrier in the beamspace. Then, the n-th entry of the deviated steering vector in (30) for the spatial location is

$$[\tilde{\mathbf{a}}(\bar{\vartheta}_{m,k}, \bar{r}_{m,k})]_n = e^{\mathrm{j}2\pi \frac{f_m}{c_0}\left((n-1)d\bar{\vartheta}_{m,k} - (n-1)^2 d^2 \bar{\Upsilon}_{m,k}\right)}, \tag{31}$$

for which we can finally define the NF beam-squint in terms of DoAs and ranges as

$$\Delta(\vartheta_k, m) = \bar{\vartheta}_{m,k} - \vartheta_k = (\eta_m - 1)\vartheta_k, \tag{32}$$

$$\Delta(r_k, m) = \bar{r}_{m,k} - r_k = (\eta_m - 1) r_k = (\eta_m - 1)\frac{1 - \eta_m^2 \vartheta_k^2}{\eta_m (1 - \vartheta_k^2)} r_k, \tag{33}$$

where $\eta_m = \frac{f_c}{f_m}$ is the ratio of the central and m-th subcarrier frequencies.

The observation of beam-squint differs when the receive array is in the NF, which is the area where the receive signal wavefront is spherical rather than plane-wave as in FF. In such a scenario, NF beam-squint causes the squint of the generated beam toward distinct locations rather than directions. As a result, handling beam-squint in the NF is even more challenging than that in the FF since the impact of beam-squint and the model mismatch due to the spherical wavefront are intertwined. Thus, NF beam-squint brings up new research challenges in both radar and communications for target/user DoA estimation [33], beamforming [28, 29], waveform design, and resource allocation [35]. One direct solution, analogous to the FF methods, is to employ OMP [37, 38] or MUSIC [33] algorithms with the dictionary of NF array responses for channel/DoA estimation and beamforming. Fig.6(b-c) shows beam-squint-aware system performance for DoA estimation root mean-squared error (RMSE) and channel estimation NMSE to account for both radar and communication scenarios, respectively [33, 49]. In both cases, it is clear that beam-squint should be accurately compensated as it leads to substantial performance loss in DoA/channel

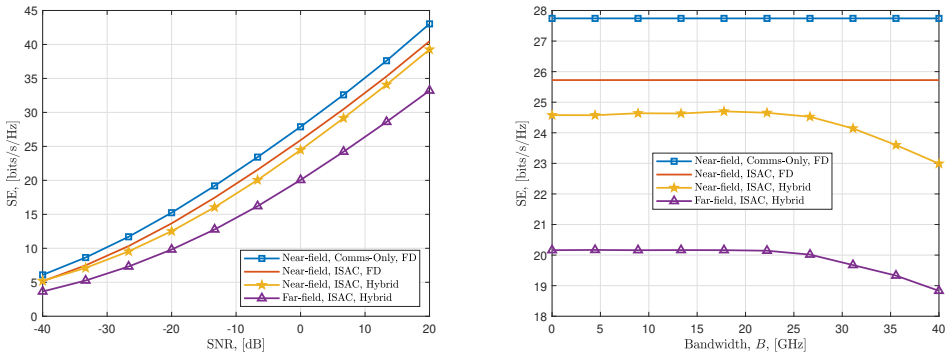

(a) (b)

Fig. 7. NF ISAC hybrid beamforming performance in terms of SE with respect to (a) SNR and (b) bandwidth. We assume $N = 128$ transmit antennas with $N_{\mathrm{RF}} = 8$ RF chains to generate beams toward $K = 3$ targets and a user with $L = 5$ NLoS paths. The carrier frequency and the bandwidth are selected as $f_c = 300$ GHz and $B = 20$ GHz, respectively.

estimation. In comparison, the model mismatch, i.e., employing only FF model for the received signal, has relatively less impact on the performance.

D. Integrated Sensing & Communications

Until recently, radar sensing and communication systems have been exclusively operated in non-overlapping frequency bands. However, a common demand for ubiquitous connectivity in wireless communications and high resolution radar sensing has led to a joint design of both systems in a shared spectrum as an effective solution: ISAC paradigms to share spectrum between radar and communications [40]. As the combination of both scenarios, NF ISAC design involves simultaneously generating multiple beams toward both users and targets which are located in the NF [39]. Fig. 7 shows the NF ISAC beamforming performance in terms of spectral efficiency (SE) with respect to both SNR as well as the system bandwidth. We can see that the FF assumption leads to serious performance degradation in both hybrid beamforming design. It can also be seen NF beam-squint should be modeled accurately to maintain satisfactory performance over a large bandwidth in the ISAC system.

V. Acoustics and Ultrasound

In acoustics and ultrasound, the source location is usually in the NF of the sensor (microphone/hydrophone for acoustics and transducer for ultrasound) array, thereby observing the wavefront curvature. Fourier near-field acoustic holography (NAH) has been very popular since 1980s [6]. This technique reconstructs a 3-D sound field from the 2-D hologram scanned above the source surface in planar, cylindrical, and

spherical geometries. This classical technique has been investigated for acoustic source localization for decades. Some recent extensions of NAH are discussed below.

A. Localization in Acoustics

Localization of acoustic signals is a major task in air/underwater communications, security surveillance and sonar, wherein acoustic vector sensor (AVS) is employed as a measuring device [8]. An AVS is composed of four components: three orthogonal velocity sensors measuring the Cartesian components and an isotropic pressure sensor measuring the acoustic pressure. Specifically, the 4×1 NF array manifold for a AVS is given by

$$\mathbf{v}=\begin{bmatrix} u \\ v \\ w \\ p \end{bmatrix}=\begin{bmatrix} \sin\varphi\cos\theta \\ \sin\varphi\sin\theta \\ \cos\varphi \\ \frac{1}{\sqrt{1+\left(\frac{\lambda}{2\pi r}\right)^2}}e^{\mathrm{j}\arctan\frac{\lambda}{2\pi r}} \end{bmatrix}, \tag{34}$$

where θ, φ and r represent azimuth/elevation angles and the distance of the source. The array manifold in (34) can be estimated via the standard subspace-based methods such as estimation of signal parameters via rotational invariance (ESPRIT) [7]. Then, the 3D source location can be estimated by taking into account the NF propagation path attenuation and the phase difference among the sensors [8].

B. Beamforming in Acoustics

In acoustics, beamforming is an important technology in microphone array signal processing to steer, shape and focus the acoustic waves toward a desired direction. A widely used beamforming technique is minimum variance distortionless response (MVDR), which is also called Capon beamforming [28]. Define $\mathbf{y}_{\mathrm{m}}(t)\in\mathbb{C}^N$ as the microphone array output, which are multiplied by the beamforming weights, i.e., $w_1,\cdots,w_N\in\mathbb{C}$. Then, the combined beamformer output is $y_o(t)=\mathbf{w}^{\mathsf{H}}\mathbf{y}_{\mathrm{m}}(t)$, where $\mathbf{y}_{\mathrm{m}}(t)=\mathbf{a}(\theta,r)s_{\mathrm{m}}(t)+\mathrm{e}_{\mathrm{m}}$ denotes the array output for the source signal $s_{\mathrm{m}}(t)\in\mathbb{C}$, and $\mathbf{w}=[w_1,\cdots,w_N]^{\mathsf{T}}$ is the beamforming vector. For a NF acoustic source signal, the MVDR beamformer design problem is

$$\underset{\mathbf{w}}{\text{minimize}}\ \mathbf{w}^{\mathsf{H}}\mathbf{R}_{\mathrm{m}}\mathbf{w}\ \ \text{subject to}\ \mathbf{w}^{\mathsf{H}}\mathbf{a}(\theta,r)=1, \tag{35}$$

where $\mathbf{R}_{\mathrm{m}}=\frac{1}{T}\sum_{t=1}^{T}\mathbf{y}_{\mathrm{m}}(t)\mathbf{y}_{\mathrm{m}}^{\mathsf{H}}(t)$ is the sample covariance matrix of the array output and $\mathbf{a}(\theta,r)$ denotes the desired direction of interest of the beamformer. The optimal solution for (35) is

$$\mathbf{w}_{\mathrm{opt}}=\left(\mathbf{a}^{\mathsf{H}}(\theta,r)\mathbf{R}_{\mathrm{m}}^{-1}\mathbf{a}(\theta,r)\right)^{-1}\mathbf{R}_{\mathrm{m}}^{-1}\mathbf{a}(\theta,r), \tag{36}$$

which requires the knowledge of $\mathbf{a}(\theta, r)$. To relax this requirement, various beamforming techniques have been introduced for a more robust design [28]. Due to simplicity of the FF model, the transformation or calibration of the NF array output to FF have been widely adopted. Therefore, in order to deal with the NF effect in acoustics, a common approach is to employ a calibration technique by applying a gain/phase compensation to each array output so that the curved wavefront of the resulting signals appear as plane-wave [12]. It is also shown in [12] that the improved beamforming performance can be achieved by exploiting the a priori knowledge of the distance between the source and the array, especially when the source of interest lies in NF while the interfering sources are located in the FF. Besides, subspace-based techniques, e.g., MUSIC and ESPRIT, can be employed for joint angle and range estimation [10].

C. Beamforming in Ultrasound Imaging

While beamforming has been widely used for narrowband signals in the FF, medical ultrasound imaging involves wideband signals originating in NF [13]. Unlike classical radar imaging that assumes targets in FF as point sources, ultrasound NF imaging encounters extended scatterers. Hence, DoA estimation algorithms designed for point sources are inapplicable here. Generally, spread source modeling approach may be employed but the presence of severe background noise precludes widespread usage of this method. Hence, MVDR beamforming is commonly used by casting the problem as spatial spectrum estimation. However, this method is very sensitive to the errors in the imaging system as it is SNR-dependent based on the data covariance matrix. In order to overcome these challenges, sidelobe pattern control techniques have been introduced based on array optimization and diagonal loading [14]. Alternatively, a full-scale electromagnetic or acoustic model of the scenario, including sensor/receiver characteristics and target environment, may be employed for DoA estimation.

Define $\mathbf{y}_{\mathrm{u}}(x_p, y_p, z_p) \in \mathbb{C}^N$ as the NF response vector at the field point (x_p, y_p, z_p) in Cartesian coordinate systems. Suppose that the the mainlobe of the array is steering to the focus point (x_f, y_f, z_f). Then, the combined beamformer output of the ultrasound transducer array from the acoustic point source at the (x_p, y_p, z_p) becomes $B(x_p, y_p, z_p) = \mathbf{w}^{\mathsf{H}}\mathbf{y}_{\mathrm{u}}(x_p, y_p, z_p)$. The aim is to achieve maximum array gain at the desired location (x_f, y_f, z_f) while minimizing the sidelobes in the beampattern. Thus, the beamforming design problem for sidelobe control is given by

$$\underset{\mathbf{w}}{\text{minimize}}\ \xi\ \ \text{subject to}\ \mathbf{w}^{\mathsf{H}}\mathbf{y}_{\mathrm{u}}(x_f, y_f, z_f) = 1, \|\mathbf{w}\| \leq \xi, |\mathbf{w}^{\mathsf{H}}\mathbf{y}_{\mathrm{u}}(x_p, y_p, z_p)| \leq \delta, \tag{37}$$

where $(x_p, y_p, z_p) \in \Theta_{\mathrm{u}}$, and δ controls the sidelobe level in the sidelobe region Θ_{u}.

VI. NF Optics

Until the 1980s, NF optics remained confined to microscopy. However, with the advent of applications such as tomography [55], cryogenic electron microscopy [56], and x-ray coherent diffractive imaging [57], NF techniques became highly diversified. In particular, infrared NF offers remarkable chemical sensitivity and nanoscopic spatial resolution, enabling the quantitative extraction of material properties from 3-D structured objects such as thin films and nanostructures [58]. A major advantage of NF imaging is its ability to surpass the resolution limits of conventional FF techniques, which are constrained by diffraction to about half the wavelength of the employed light. This limitation is a significant barrier to examining nanoscale objects, where resolutions in the range of 10-100 nm are required. In contrast, NF propagation enables resolutions that are unattainable with traditional methods, especially in the holographic regime, where small Fresnel numbers produce high contrast. More recently, there has been a focus on NF phase Retrieval (PR) for fields such as spanning holography [59], ptychography [60], and lens-less x-ray coherent diffractive imaging [57].

A general NF PR problem has the following setting. The spherical near-field samples are defined in the rotation space, which is a set of all possible rotations on the 3-D Euclidean space $\mathbb{R}^3$. This space is parameterized by three rotation angles: polarization angles, $\phi, \chi \in [02\pi]$ and azimuth angle $\theta \in [0\pi]$. Wigner D-functions are the orthonormal basis of this space, i.e., [61]

$$\mathrm{D}_l^{k,n}(\theta,\phi,\chi) = N_l e^{-\mathrm{j}k\phi}\mathrm{d}_l^{k,n}(\cos\theta)e^{-\mathrm{j}n\chi}, \tag{38}$$

where $\mathrm{d}_l^{k,n}(\cos\theta)$ is the Wigner D-function of band-limit degree $0 \le l \le B-1$ and orders $-l \le k, n \le l$, and $N_l = \sqrt{\frac{2l+1}{8\pi^2}}$ is the normalization factor. The spherical NF field $h(\theta,\phi,\chi)$ using a Wigner D-function expansion and bandwidth B is

$$h(\theta,\phi,\chi) = \sum_{l=0}^{B-1}\sum_{k=-l}^{l}\sum_{n=-l}^{l}\alpha_l^{k,n}\mathrm{D}_l^{k,n}(\theta,\phi,\chi), \tag{39}$$

where $\{\alpha_l^n\}_{k,n=-l}^{l}$ are spherical mode coefficients to be reconstructed. Spherically sampling $\{\theta,\phi,\chi\}$ in m points, the Wigner D expansion (39) is rewritten in the form of following linear feasibility problem: $\mathbf{h} = \mathbf{A}_W\boldsymbol{\alpha}$, where $\mathbf{h} = \left[h\left(\theta_1,\phi_1,\chi_1\right),\cdots,h\left(\theta_m,\phi_m,\chi_m\right)\right]^\top, \boldsymbol{\alpha} \in \mathbb{C}^n$ is constructed by Wigner D coefficients $\{\alpha_l^n\}_{k,n=-l}^{l}$, and the Wigner D-matrix $\mathbf{A}_W$ is

$$\mathbf{A}_W = \begin{pmatrix} \mathrm{D}_0^{0,0}\left(\theta_1,\phi_1,\chi_1\right) & \cdots & \mathrm{D}_{B-1}^{B-1,B-1}\left(\theta_1,\phi_1,\chi_1\right) \\ \vdots & \vdots & \ddots & \vdots \\ \mathrm{D}_0^{0,0}\left(\theta_m,\phi_m,\chi_m\right) & \cdots & \mathrm{D}_{B-1}^{B-1,B-1}\left(\theta_m,\phi_m,\chi_m\right) \end{pmatrix}. \tag{40}$$

This matrix is a collection of m different samples of Wigner D-functions, where for each sample there exist Wigner D-functions related to its degree l and order $|k|,|n| < B$. When only the phaseless measurements

of NF radiation are available, then recovering $\boldsymbol{\alpha}$ from the embedded phaseless data given the knowledge of $\mathbf{A}_W$ is the optimization problem

$$\text{Find } \boldsymbol{\alpha} \quad \text{subject to} \quad \boldsymbol{y} = |\mathbf{A}_W \boldsymbol{\alpha}|, \tag{41}$$

where the non-convex constraint models the measurement process. This PR problem may also be generalized to mixed measurements from near-, middle-, and far-zone fields [62]. Since the problem results in a non-convex inverse problem, the recovery method to obtain the phase generally exploit a specific optical design or signal structure [62, 63].

VII. Summary and Future Outlook

NF signal processing, traditionally regarded as a specialized niche, has a rich and extensive history that has significantly contributed to the advancement of various scientific fields, including electromagnetics, acoustics, and medical imaging. Classical NF techniques laid the groundwork for understanding and manipulating electromagnetic fields at close ranges, enabling breakthroughs that have shaped modern technology. In recent years, however, there has been a remarkable resurgence of interest in NF signal processing, driven by advancements in emerging technologies such as ELAA and ISAC. Further, enhanced capabilities for conducting measurements across various optical regimes have reinvigorated NF optics, leading to a proliferation of specialized applications. Recent quantum-inspired techniques like those utilizing Rydberg atoms [64] have underscored the need to revisit and expand NF signal processing approaches. In summary, the ongoing exploration of NF theory and its applications holds great promise for addressing new and complex problems in signal processing.

References

[1] C. A. Balanis, *Modern antenna handbook*. John Wiley & Sons, 2011.

[2] D. W. Pohl and D. Courjon, *Near field optics*, ser. NATO Science Series E. Springer, 2012, vol. 242.

[3] C. Jahncke, H. Hallen, and M. Paesler, "Nano-raman spectroscopy and imaging with a near-field scanning optical microscope," *Journal of Raman spectroscopy*, vol. 27, no. 8, pp. 579–586, 1996.

[4] D. Kurouski, A. Dazzi, R. Zenobi, and A. Centrone, "Infrared and Raman chemical imaging and spectroscopy at the nanoscale," *Chem. Soc. Rev.*, vol. 49, no. 11, pp. 3315–3347, Jun. 2020.

[5] W.-T. Su, Y.-C. Hung, P.-J. Yu, C.-W. Lin, and S.-H. Yang, "Physics-Guided Terahertz Computational Imaging: A tutorial on state-of-the-art techniques," *IEEE Signal Process. Mag.*, vol. 40, no. 2, pp. 32–45, Feb. 2023.

[6] M. R. Bai, J.-G. Ih, and J. Benesty, *Acoustic array systems: Theory, implementation, and application*. John Wiley & Sons, 2013.

[7] Y. I. Wu, K. T. Wong, and S.-K. Lau, "The Acoustic Vector-Sensor's Near-Field Array-Manifold," *IEEE Trans. Signal Process.*, vol. 58, no. 7, pp. 3946–3951, Apr. 2010.

[8] T. Shu, J. He, and V. Dakulagi, "3-D Near-Field Source Localization Using a Spatially Spread Acoustic Vector Sensor," *IEEE Trans. Aerosp. Electron. Syst.*, vol. 58, no. 1, pp. 180–188, Jun. 2021.

[9] H. Lee, J. Ahn, Y. Kim, and J. Chung, "Direction-of-arrival estimation of far-field sources under near-field interferences in passive sonar array," *IEEE Access*, vol. 9, pp. 28 413–28 420, 2021.

[10] L. Kumar and R. M. Hegde, "Near-Field Acoustic Source Localization and Beamforming in Spherical Harmonics Domain," *IEEE Trans. Signal Process.*, vol. 64, no. 13, pp. 3351–3361, Mar. 2016.

[11] T. He, Q. Pan, Y. Liu, X. Liu, and D. Hu, "Near-field beamforming analysis for acoustic emission source localization," *Ultrasonics*, vol. 52, no. 5, pp. 587–592, Jul. 2012.

[12] J. G. Ryan and R. A. Goubran, "Array optimization applied in the near field of a microphone array," *IEEE Trans. Speech Audio Processing*, vol. 8, no. 2, pp. 173–176, Mar. 2000.

[13] F. Viola, M. A. Ellis, and W. F. Walker, "Time-Domain Optimized Near-Field Estimator for Ultrasound Imaging: Initial Development and Results," *IEEE Trans. Med. Imaging*, vol. 27, no. 1, pp. 99–110, Dec. 2007.

[14] Z. He, F. Zheng, Y. Ma, H. H. Kim, Q. Zhou, and K. K. Shung, "A sidelobe suppressing near-field beamforming approach for ultrasound array imaging," *J. Acoust. Soc. Am.*, vol. 137, no. 5, p. 2785, May 2015.

[15] T. K. Sarkar, M. Salazar-Palma, and E. L. Mokole, *Physics of Multiantenna Systems and Broadband Processing*. John Wiley & Sons, 2008.

[16] A. M. Molaei, P. del Hougne, V. Fusco, and O. Yurduseven, "Efficient Joint Estimation of DOA, Range and Reflectivity in Near-Field by Using Mixed-Order Statistics and a Symmetric MIMO Array," *IEEE Trans. Veh. Technol.*, vol. 71, no. 3, pp. 2824–2842, Dec. 2021.

[17] B. Friedlander, "Localization of Signals in the Near-Field of an Antenna Array," *IEEE Trans. Signal Process.*, vol. 67, no. 15, pp. 3885–3893, Jun. 2019.

[18] C. Cheng, S. Liu, H. Wu, and Y. Zhang, "An Efficient Maximum-Likelihood-Like Algorithm for Near-Field Coherent Source Localization," *IEEE Trans. Antennas Propag.*, vol. 70, no. 7, pp. 6111–6116, Mar. 2022.

[19] A. M. Elbir and T. E. Tuncer, "Far-field DOA estimation and near-field localization for multipath signals," *Radio Sci.*, vol. 49, no. 9, pp. 765–776, Sep. 2014.

[20] I. Podkurkov, G. Seidl, L. Khamidullina, A. Nadeev, and M. Haardt, "Tensor-Based Near-Field Localization Using Massive Antenna Arrays," *IEEE Trans. Signal Process.*, vol. 69, pp. 5830–5845, Aug. 2021.

[21] H. Wang, Z. Xiao, and Y. Zeng, "Cramér-Rao Bounds for Near-Field Sensing with Extremely Large-Scale MIMO," *IEEE Trans. Signal Process.*, pp. 1–15, Jan. 2024.

[22] J. Liang and D. Liu, "Passive Localization of Mixed Near-Field and Far-Field Sources Using Two-stage MUSIC Algorithm," *IEEE Trans. Signal Process.*, vol. 58, no. 1, pp. 108–120, Aug. 2009.

[23] Z. Zheng, M. Fu, W.-Q. Wang, S. Zhang, and Y. Liao, "Localization of Mixed Near-Field and Far-Field Sources Using Symmetric Double-Nested Arrays," *IEEE Trans. Antennas Propag.*, vol. 67, no. 11, pp. 7059–7070, Jul. 2019.

[24] R. Schmidt, "Multiple emitter location and signal parameter estimation," *IEEE Trans. Antennas Propag.*, vol. 34, no. 3, pp. 276–280, Mar. 1986.

[25] M. Haardt, R. N. Challa, and S. Shamsunder, "Improved bearing and range estimation via high-order subspace based Unitary ESPRIT," in *Conference Record of The Thirtieth Asilomar Conference on Signals, Systems and Computers*. IEEE, pp. 03–06.

[26] N. Yuen and B. Friedlander, "Performance analysis of higher order ESPRIT for localization of near-field sources," *IEEE Trans. Signal Process.*, vol. 46, no. 3, pp. 709–719, Mar. 1998.

[27] A. Sakhnini, S. De Bast, M. Guenach, A. Bourdoux, H. Sahli, and S. Pollin, "Near-Field Coherent Radar Sensing Using a Massive MIMO Communication Testbed," *IEEE Trans. Wireless Commun.*, vol. 21, no. 8, pp. 6256–6270, Feb. 2022.

[28] A. M. Elbir, K. V. Mishra, S. A. Vorobyov, and R. W. Heath, "Twenty-Five Years of Advances in Beamforming: From convex and nonconvex optimization to learning techniques," *IEEE Signal Process. Mag.*, vol. 40, no. 4, pp. 118–131, Jun. 2023.

[29] E. Björnson, Ö. T. Demir, and L. Sanguinetti, "A Primer on Near-Field Beamforming for Arrays and Reconfigurable Intelligent Surfaces," in *2021 55th Asilomar Conference on Signals, Systems, and Computers*, 2021, pp. 2021–03.

[30] Z. Wang, J. Zhang, H. Du, D. Niyato, S. Cui, B. Ai, M. Debbah, K. B. Letaief, and H. V. Poor, "A Tutorial on Extremely Large-Scale MIMO for 6G: Fundamentals, Signal Processing, and Applications," *IEEE Commun. Surv. Tutorials*, p. 1, Jan. 2024.

[31] Y. Liu, Z. Wang, J. Xu, C. Ouyang, X. Mu, and R. Schober, "Near-Field Communications: A Tutorial Review," *IEEE Open J. Commun. Soc.*, vol. 4, pp. 1999–2049, Aug. 2023.

[32] M. Cui, Z. Wu, Y. Lu, X. Wei, and L. Dai, "Near-Field MIMO Communications for 6G: Fundamentals, Challenges, Potentials, and Future Directions," *IEEE Commun. Mag.*, vol. 61, no. 1, pp. 40–46, Sep. 2022.

[33] A. M. Elbir, K. V. Mishra, and S. Chatzinotas, "Spherical Wavefront Near-Field DoA Estimation in THz Automotive Radar," in *2024 18th European Conference on Antennas and Propagation (EuCAP)*, 2024, pp. 2024–03.

[34] Y. Lu and L. Dai, "Near-Field Channel Estimation in Mixed LoS/NLoS Environments for Extremely Large-Scale MIMO Systems," *IEEE Trans. Commun.*, vol. 71, no. 6, pp. 3694–3707, Mar. 2023.

[35] N. J. Myers and R. W. Heath, "InFocus: A Spatial Coding Technique to Mitigate Misfocus in Near-Field LoS Beamforming," *IEEE Trans. Wireless Commun.*, vol. 21, no. 4, pp. 2193–2209, Sep. 2021.

[36] A. M. Elbir, A. Celik, and A. M. Eltawil, "Near-field Hybrid Beamforming for Terahertz-band Integrated Sensing and Communications," in *2023 IEEE Globecom Workshops (GC Wkshps)*, 2023, pp. 04–08.

[37] S. Yang, W. Lyu, Z. Hu, Z. Zhang, and C. Yuen, "Channel Estimation for Near-Field XL-RIS-Aided mmWave Hybrid Beamforming Architectures," *IEEE Trans. Veh. Technol.*, vol. 72, no. 8, pp. 11 029–11 034, Mar. 2023.

[38] A. M. Elbir, K. V. Mishra, and S. Chatzinotas, "NBA-OMP: Near-Field Beam-Split-Aware Orthogonal Matching Pursuit for Wideband THz Channel Estimation," in *ICASSP 2023 - 2023 IEEE International Conference on Acoustics, Speech and Signal Processing (ICASSP)*, 2023, pp. 04–10.

[39] Z. Wang, X. Mu, and Y. Liu, "Near-Field Integrated Sensing and Communications," *IEEE Commun. Lett.*, vol. 27, no. 8, pp. 2048–2052, May 2023.

[40] A. M. Elbir, K. V. Mishra, and S. Chatzinotas, "Terahertz-Band Joint Ultra-Massive MIMO Radar-Communications: Model-Based and Model-Free Hybrid Beamforming," *IEEE J. Sel. Top. Signal Process.*, vol. 15, no. 6, pp. 1468–1483, Oct. 2021.

[41] L. Khamidullina, I. Podkurkov, and M. Haardt, "Conditional and Unconditional Cramér-Rao Bounds for Near-Field Localization in Bistatic MIMO Radar Systems," *IEEE Trans. Signal Process.*, vol. 69, pp. 3220–3234, May 2021.

[42] W. Lv, K. V. Mishra, and S. Chen, "Co-pulsing FDA radar," *IEEE Transactions on Aerospace and Electronic Systems*, vol. 59, no. 2, pp. 1107–1126, 2023.

[43] P. Vouras, K. V. Mishra, A. Artusio-Glimpse, S. Pinilla, A. Xenaki, D. W. Griffith, and K. Egiazarian, "An overview of advances in signal processing techniques for classical and quantum wideband synthetic apertures," *IEEE Journal of Selected Topics in Signal Processing*, vol. 17, no. 2, pp. 317–369, 2023.

[44] B. Wang, Y. Zhao, and J. Liu, "Mixed-Order MUSIC Algorithm for Localization of Far-Field and Near-Field Sources," *IEEE Signal Process. Lett.*, vol. 20, no. 4, pp. 311–314, Feb. 2013.

[45] X. Su, P. Hu, Z. Liu, T. Liu, B. Peng, and X. Li, "Mixed Near-Field and Far-Field Source Localization Based On Convolution Neural Networks via Symmetric Nested Array," *IEEE Trans. Veh. Technol.*, vol. 70, no. 8, pp. 7908–7920, Jul. 2021.

[46] B. Friedlander and A. J. Weiss, "Direction finding using spatial smoothing with interpolated arrays," *IEEE Trans. Aerosp. Electron. Syst.*, vol. 28, no. 2, pp. 574–587, Apr. 1992.

[47] H. Lu, Y. Zeng, C. You, Y. Han, J. Zhang, Z. Wang, Z. Dong, S. Jin, C.-X. Wang, T. Jiang, X. You, and R. Zhang, "A Tutorial on Near-Field XL-MIMO Communications Towards 6G," *arXiv*, Oct. 2023.

[48] G. C. Nwalozie, D. Rakhimov, and M. Haardt, "Near-Field Beamforming for MU-MIMO Millimeter Wave Communication System," in *2023 31st European Signal Processing Conference (EUSIPCO)*, 2023, pp. 04–08.

[49] A. M. Elbir, W. Shi, A. K. Papazafeiropoulos, P. Kourtessis, and S. Chatzinotas, "Terahertz-Band Channel and Beam Split Estimation via Array Perturbation Model," *IEEE Open J. Commun. Soc.*, p. 1, Mar. 2023.

[50] M. Cui and L. Dai, "Channel Estimation for Extremely Large-Scale MIMO: Far-Field or Near-Field?" *IEEE Trans. Commun.*, vol. 70, no. 4, pp. 2663–2677, Jan. 2022.

[51] Ö. T. Demir, A. Kosasih, and E. Björnson, "Spatial Correlation Modeling and RS-LS Estimation of Near-Field Channels with Uniform Planar Arrays," *arXiv*, Jun. 2024.

[52] E. Björnson *et al.*, "Towards 6G MIMO: Massive Spatial Multiplexing, Dense Arrays, and Interplay Between Electromagnetics and Processing," *arXiv*, Jan. 2024.

[53] G. Bacci, L. Sanguinetti, and E. Björnson, "Spherical wavefronts improve MU-MIMO spectral efficiency when using electrically large arrays," *IEEE Wireless Communications Letters*, vol. 12, no. 7, pp. 1219–1223, 2023.

[54] A. M. Elbir, K. V. Mishra, A. Celik, and A. M. Eltawil, "The Curse of Beam-Squint in ISAC: Causes, Implications, and Mitigation Strategies," *IEEE Commun. Magazine, in press*, Jun. 2024.

[55] P. S. Carney, V. A. Markel, and J. C. Schotland, "Near-field tomography without phase retrieval," *Physical review letters*, vol. 86, no. 26, p. 5874, 2001.

[56] G. Zickert and S. Maretzke, "Cryogenic electron tomography reconstructions from phaseless data," *Inverse Problems*, vol. 34, no. 12, p. 124001, 2018.

[57] A.-L. Robisch and T. Salditt, "Phase retrieval for object and probe using a series of defocus near-field images," *Optics Express*, vol. 21, no. 20, pp. 23 345–23 357, 2013.

[58] A. A. Govyadinov, S. Mastel, F. Golmar, A. Chuvilin, P. S. Carney, and R. Hillenbrand, "Recovery of permittivity and depth from near-field data as a step toward infrared nanotomography," *ACS Nano*, vol. 8, no. 7, pp. 6911–6921, 2014.

[59] J. Hagemann and T. Salditt, "Divide and update: Towards single-shot object and probe retrieval for near-field holography," *Optics Express*, vol. 25, no. 18, pp. 20 953–20 968, 2017.

[60] H. Zhang, S. Jiang, J. Liao, J. Deng, J. Liu, Y. Zhang, and G. Zheng, "Near-field Fourier ptychography: Super-resolution phase retrieval via speckle illumination," *Optics Express*, vol. 27, no. 5, pp. 7498–7512, 2019.

[61] E. Wigner, *Gruppentheorie und ihre Anwendung auf die Quantenmechanik der Atomspektren*. Springer, 1931, in German.

[62] S. Pinilla, K. V. Mishra, I. Shevkunov, M. Soltanalian, V. Katkovnik, and K. Egiazarian, "Unfolding-Aided Bootstrapped Phase Retrieval in Optical Imaging: Explainable AI reveals new imaging frontiers," *IEEE Signal Process. Mag.*, vol. 40, no. 2, pp. 46–60, Feb. 2023.

[63] R. Jacome, K. V. Mishra, B. M. Sadler, and H. Arguello, "An invitation to hypercomplex phase retrieval: Theory and applications," *IEEE Signal Process. Mag.*, 2024, in press.

[64] P. Vouras, K. V. Mishra, and A. Artusio-Glimpse, "Phase retrieval for Rydberg quantum arrays," in *IEEE International Conference on Acoustics, Speech and Signal Processing*, 2023, pp. 1–5.